

K-shell spectroscopy of silicon ions as diagnostic for high electric fields

R. Loetzsch,^{1,2,a)} O. Jäckel,^{1,2} S. Höfer,^{1,2} T. Kämpfer,^{1,2} J. Polz,² I. Uschmann,^{1,2}
M. C. Kaluza,^{1,2} E. Förster,¹ E. Stambulchik,³ E. Kroupp,³ and Y. Maron³

¹Helmholtz-Institut Jena, Helmholtzweg 4, D-07743 Jena, Germany

²Institut für Optik und Quantenelektronik, Friedrich-Schiller-Universität Jena, Max-Wien-Platz 1,
07743 Jena, Germany

³Faculty of Physics, Weizmann Institute of Science, P.O. Box 26, Rehovot 76100, Israel

(Received 22 February 2012; accepted 30 October 2012; published online 28 November 2012)

We developed a detection scheme, capable of measuring X-ray line shape of tracer ions in μm thick layers at the rear side of a target foil irradiated by ultra intense laser pulses. We performed simulations of the effect of strong electric fields on the K-shell emission of silicon and developed a spectrometer dedicated to record this emission. The combination of a cylindrically bent crystal in von Hámos geometry and a CCD camera with its single photon counting capability allows for a high dynamic range of the instrument and background free spectra. This approach will be used in future experiments to study electric fields of the order of TV/m at high density plasmas close to solid density. © 2012 American Institute of Physics. [<http://dx.doi.org/10.1063/1.4767452>]

I. INTRODUCTION

During the interaction of an intense laser pulse having an intensity larger than 10^{18} W/cm² with solid targets, electrons are accelerated to relativistic energies. This is accompanied by the creation of strong electric and magnetic fields, reaching TV/m and tens of kT, either directly by strong currents or by charge separation effects.^{1,2} The latter is especially apparent at the rear side of laser irradiated foils where it leads to the acceleration of ions up to MeV energy, known as target normal sheath acceleration (TNSA).¹ Although the impacts of these strong fields are well known and used, most of the information about the fields is gained through simulations, since they are difficult to measure. However, measurements would be very helpful to verify and benchmark these simulations, which are important not only for the understanding of laser foil experiments but also of astrophysical and fusion plasmas.^{3,4} Experimental insight into these transient processes is typically gathered via probing of the electron population with optical light methods in transversal⁵ or reflection geometry,⁶ as well as by proton deflectometry.^{7,8} While the first could only measure the electron density with high temporal and spatial resolution, the latter is also sensitive to magnetic fields.⁹ Later on proton deflectometry was developed as an ultrafast technique to track high field fronts close to the speed of light.¹⁰ Here we report on a method that allows for measuring directly the electric fields.

This method is based on X-ray spectroscopy of the self emission of atoms exposed to the fields, affected by the Stark effect. As a unique measure of the fields, we use the relative intensity of the forbidden L₁-K transition, that becomes partially allowed in these strong fields. Thus, we use targets with tracer layers deposited on the rear side and record their self emission.

II. SIMULATIONS

The TNSA process, which leads to efficient ion acceleration during the interaction of an intense laser pulse with solid targets, can be described as follows. The laser pulse creates, mainly via the ponderomotive force, a hot electron population that propagates through the foil. This electron population could be described in the first approximation by a Boltzmann distribution with an effective temperature determined by the ponderomotive potential of the laser pulse.^{5,11} This leads to an exponentially decaying electron density in target normal direction at the target rear side with a characteristic length scale λ_d , the Debye length. With some assumptions for the electron beam divergence, the conversion of laser energy into hot electrons, a laser intensity of 10^{19} W/cm² and a target thickness of $6 \mu\text{m}$, the electric field strength could be estimated by ~ 1 TV/m and the Debye length by $\sim 0.6 \mu\text{m}$.⁵

The Stark effect due to sufficiently strong electric fields induces shifts of energy levels and mixing of eigenstates with different parities. This mixing results in the appearance of so-called “forbidden lines,” i.e., transitions that are forbidden in the dipole approximation due to the selection rules. Forbidden transitions have been successfully used in the visible and UV spectral regions for unambiguous determination of electric fields, both ac and dc, in plasmas.^{12,13} Here, we employ this technique in the X-ray region. Specifically, we simultaneously measure the forbidden L₁-K and the allowed L_{2,3}-K, i.e., K α , inner-shell transitions of silicon.

Due to the strong electric fields, which are expected in the range of 0.1–1 TV/m, Si charge states with electron configurations including $n = 3$ (*M*-shell) states are fully ionized. Indeed, the classical ionization limit of a hydrogen-like ion with core charge Z_{core} is in atomic units:

$$F_i = \frac{Z_{\text{core}}^3}{16n^4}, \quad (1)$$

(see, e.g., Ref. 14) and is further reduced due to the quantum tunneling. For the $n = 2$ configurations, one estimates

^{a)}Electronic mail: robert.loetzsch@uni-jena.de.

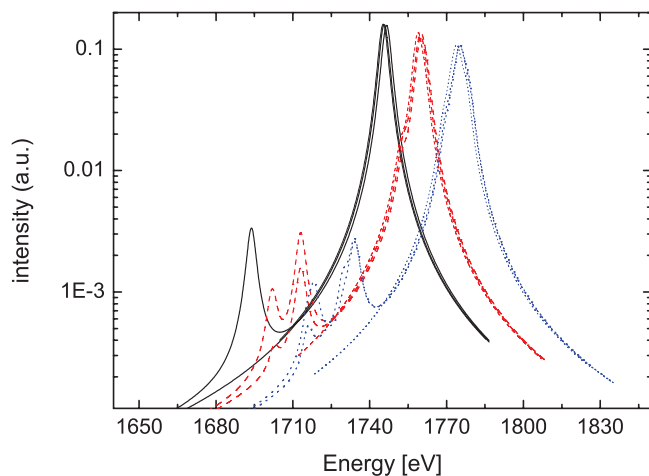


FIG. 1. Spectra of the inner-shell transitions of three Si charge states. Thin lines: No electric field; thick lines: $F = 0.5$ TV/m is assumed. The strong allowed $K\alpha$ and the weak, induced by the electric field, forbidden L_1 -K transitions are seen. The line shapes are area-normalized.

the critical fields of ~ 0.4 TV/m, 0.7 TV/m, and 1 TV/m for Si(VI), Si(VII), and Si(VIII) charge states, respectively. However, due to the highly transient nature of the TNSA fields ($\sim 10^{-12}$ s) and very high $K\alpha$ radiative rates ($\sim 10^{13}$ s $^{-1}$), it is expected that a mixture of spectroscopic signatures of all of these charge states will be present.

The influence of the TNSA electric field on the surviving Si charge states results in two effects. First, the energies of the atomic levels shift, resulting in shifting and splitting of radiative transitions. Second, the otherwise forbidden L_1 -K transition becomes partially allowed due to the mixture of electronic states with different parities. We performed the calculations using the flexible atomic code (FAC)¹⁵ and the method described in Ref. 16, with nearly identical results. The atomic data used in both cases were calculated by FAC. In Figure 1, the Stark profiles of the L-K transitions of the three Si charge states are shown alongside the zero-field profiles. The dynamic Stark broadening was not calculated, however, the static Stark profiles were convolved with an effective 2 eV Lorentzian in order to account for it approximately. An exact value of the dynamic broadening is irrelevant for the method, as will follow from the discussion below.

For the electric field strengths considered in this study, both effects, the Stark shifts and the ratio of the forbidden-to-allowed line intensities, depend quadratically on the TNSA field and thus allowing for inferring the latter. For a field of 0.1 TV/m, for instance, the forbidden line would be 25 times weaker than shown in Figure 1. However, the use of the line shifts is unreliable, due to the relatively small values of the shifts, as it can be seen in Figure 1. In addition, any field distribution would result in further smearing of the lines (both the allowed and the forbidden ones). Contrary to that, the forbidden lines of the Si(VI) and Si(VII) charge states appear in the region free of other spectral features, and therefore can serve as a reliable indication of the electric fields. We note that without the electric field, the radiative rate of the L_1 -K line (and hence its intensity), determined by the magnetic dipole (M1) transition, is $\sim 10^{-6}$ times lower than that of the elec-

tric dipole (E1) of $K\alpha$, which is significantly smaller than the electric-field-induced ratio.

It should be expected that $K\alpha$ radiation from regions without strong electric fields ($\lesssim 0.1$ TV/m), where lower than Si(VI) charge states may be present, contributes to the measured spectrum. Such a radiation is spectrally very close to the Si(VI) $K\alpha$ line, since electrons in the M -shell almost do not affect the inner electrons. Thus, it has no negative impact on the detection of the Si(VI) and Si(VII) forbidden components. It would only alter the ratio from the forbidden to the $K\alpha$ line. Since one has to expect the electric field to decline much more rapidly inside the target than outside,¹⁷ only a few hundred nm of the silicon layer would experience the field. The ratio of Si(VII) forbidden line to its $K\alpha$ component would not be altered by the finite extend of the electric field inside the target, if one assumes Si(VII) to be produced mainly by field ionization.

Excited-state satellites of Si(VI) may be present if the bulk electron temperature is sufficiently high ($\gtrsim 10$ eV), however, their energies lie in the “blue” part of the spectrum, close to the next-charge-state Si(VII) $K\alpha$ transition,¹⁸ again not affecting the sensitivity of the method. Finally, minor energy shifts (~ 1 eV) due to the chemical composition,¹⁹ which should be considered, since we use silicon monoxide instead of the atomic silicon assumed in the calculations, are negligible as well.

Finally, it should be noted that the forbidden transition is polarized. For the Si(VI) charge state, in which we are mainly interested in, the emitted radiation is linearly polarized in the direction of the electric field, i.e., the target normal. For the higher charged ions, the different polarization components are mixed. For the spectra shown in Figure 1, the polarization components are averaged.

Thus, we want to measure a signal ~ 2 – 3 orders of magnitude smaller than the $K\alpha$ emission. Therefore, we need a very bright spectrometer and an efficient background reduction.

III. SPECTROMETER

The design of the spectrometer followed two main considerations. First, in order to measure the rather weak signals in the energy range around 1700 eV, a spectrometer with a high collection efficiency for the isotropically emitted radiation has to be utilized. The energy resolution needs to be only moderate, but the spectrometer has to cover the emission in a wide energy range of ~ 100 eV. These requirements are met by a von Hámos spectrometer with crystals providing large lattice plane distances like pentaerythrite (PET). PET crystals are well known in X-ray spectroscopy having high integrated reflectivities and low background due to their low Z elements.

Second, in experiments at ultrahigh laser intensities, a huge amount of background radiation from direct and scattered hard X-rays, fluorescence radiation, and from the hot electrons has to be handled. This background must not only be addressed by passive shielding, but also by an appropriate detection scheme. We use a charged coupled device (CCD) camera operated in the single photon counting regime.^{20–22} This allows for distinguishing between signal and noise efficiently.

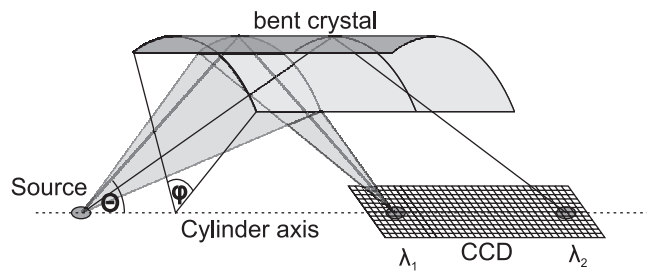


FIG. 2. Scheme of the von Hámós spectrometer: Source and detector are located on the axis of the cylindrically bent crystal. Each wavelength is reflected with a Bragg angle Θ by a sector on the crystal surface and refocused onto a point on the axis. φ is the aperture angle of the cylindrically bent crystal.

The spectrometer utilizes the von Hámós scheme, depicted in Figure 2. In our case, the crystal only focusses the radiation, without imaging resolution in the direction perpendicular to the dispersion, which is in principle possible in the von Hámós scheme. This is caused by the limited degree of perfection of the used crystal. The crystal has a bending radius R of 100 mm and an opening angle φ of 29° . The 002 PET reflection ($2d_{002} = 8.742 \text{ \AA}$) is used. This gives a Bragg angle of 54.7° for the $K\alpha$ line and a source-detector distance $l = 2R/\tan \Theta$ of 142 mm. The dispersion on the cylinder axis amounts to

$$\frac{\Delta x}{\Delta \lambda} = \frac{l}{\lambda \cot \Theta}.$$

The energy resolution of the spectrometer is dominated by the crystal perfection and amounts to $\sim 1 \text{ eV}$. At this Bragg angle around 55° , the reflected radiation is partially polarized. PET crystals are known to have a reflectivity according to the dynamical theory of X-ray diffraction when they are used shortly after production. This amounts to 2.9×10^{-4} and 0.7×10^{-4} rad for the σ and π -component at 1740 keV, respectively. But it is also known that they are aging²³ with the integrated reflectivity tending towards the kinematical limit,²⁴ which is 1.2×10^{-3} and 0.13×10^{-3} rad for the σ and π -components, respectively. The crystal used here is 20 years old. The collection efficiency η for the von Hámós scheme, i.e., the fraction N_{coll} of the emitted photons N_{em} that are collected in the image plane, is given by

$$\eta = \frac{N_{\text{coll}}}{N_{\text{em}}} = \frac{R_i \Omega}{4\pi} = \frac{R_i \varphi R}{4\pi l_a}, \quad (2)$$

where Ω is the aperture angle perpendicular to the dispersion plane covered by the crystal, l_a the distance source-crystal, and R_i the crystal's integrated reflectivity. For unpolarized radiation, η amounts to 1×10^{-5} (4×10^{-5}) for the integrated reflectivities according to the dynamical (kinematical) theory. For the spectrometer detection efficiency, the transmission of the two light protection foils consisting in all of $9 \mu\text{m}$ Mylar and $0.6 \mu\text{m}$ Al and the quantum efficiency of the CCD have to be taken into account. They amount to 0.45 and 0.7, respectively.

To operate the CCD camera at this short distance from the laser-generated plasma, great efforts on shielding have to be made. To reduce the hard X-ray self emission of the spectrometer induced by fluorescence and scattering, the spectrometer

housing was built from a massive PMMA block, where only the beam path from the plasma to the crystal and from the crystal to the CCD camera was cut out. Electrons propagating in the direction of the crystal were blocked by a magnetic field of a magnetic yoke. The camera was housed in a double wall cage consisting of 1 cm thick plastic and 4 mm thick brass. Additional 5 cm lead and 3 cm PMMA were placed between the plasma and the CCD.

The single photon counting regime of the CCD detection allows only for a limited photon flux, i.e., the averaged number of photons per pixel must be smaller than 0.1. The von Hámós scheme allows to adjust the photon flux on the detector without changing the total amount of detected photons and without changing the spectral resolution. Therefore, only the distance between the crystal and the detector has to be changed. To validate this approach, we calculated the image in the detector plane via ray tracing methods.²⁵ Therefore, a monochromatic source was assumed and the distance between crystal and detector was varied around the optimal distance of 122.6 mm. The crystal reflection curve was calculated according to the dynamical theory. The results are shown in Figure 3. The photon flux could be tuned by ~ 2 orders of magnitude.

Since radiation of different wavelengths is reflected by different arcs of the crystal surface, the spectrometer was first tested in terms of homogeneity of the reflection. A silicon $K\alpha$ line emitter was realized by irradiating the edge of a silicon wafer with continuum radiation from a tungsten X-ray tube. By placing this $0.5 \times 70 \text{ mm}^2$ sized source on the cylinder axis of the crystal, we could record the reflection from the whole crystal on a film, placed also on the cylinder axis of the crystal. The efficiency of the spectrometer varies by less than 20%.

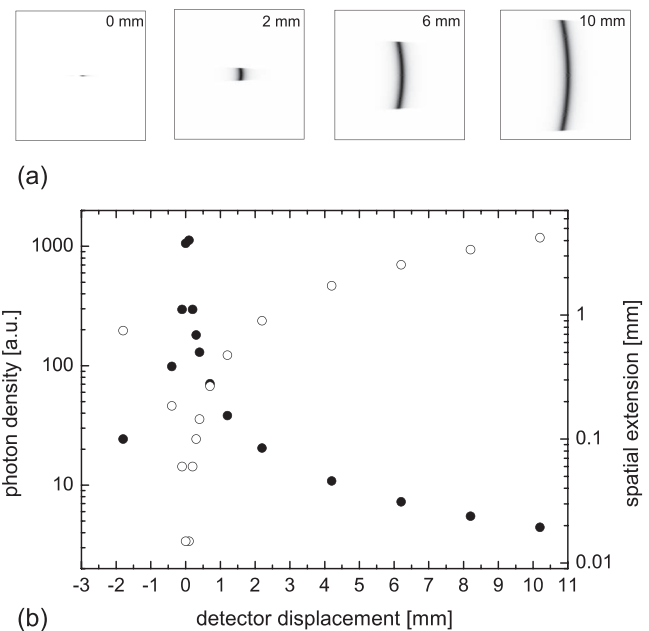


FIG. 3. Ray tracing simulations of the image of a monochromatic point source with the detector at variable distances from the crystal focus. Panel (a) shows these images, their sizes are 5 mm in both directions. The horizontal direction is the dispersion direction. Panel (b) shows the maximum photon flux (full symbols) in the images and the spatial extent (open symbols).

IV. EXPERIMENT

To measure the L_1 -K transition, two geometrical constraints have to be fulfilled, which are depicted in Figure 4. First, this transition is polarized in the direction of the inducing electric field, which is expected to be normal to the target surface, while the $K\alpha$ emission is unpolarized. Second, the crystal spectrometer mainly reflects s-polarized radiation, since it is used at a Bragg angle of 54° . Thus, the angle between the dispersion plane of the spectrometer and the target normal ψ should be as large as possible, and the angle between the direction to the spectrometer crystal and the target surface ξ should be as small as possible. The ratio of the detected intensity for the unpolarized and the polarized component depends on ψ and ξ such as

$$\frac{I_{\text{unpol}}}{I_{\text{pol}}} = \frac{1 + K}{\sin \psi + K \cos \psi \cos \xi}, \quad (3)$$

while K is $|\cos(2\Theta)|$ for the dynamical theory and $\cos^2(2\Theta)$ for the kinematical theory. Both angles are limited due to space and spectrometer design. The values in the experiment were $\psi = 50^\circ$ and $\xi = 45^\circ$. For these values the ratio of detected intensity for the unpolarized and polarized component amounts to 1.37 (1.47) for the crystal reflection according to the dynamical (kinematical) theory.

The experiments were performed at the Jena 30 TW titanium:sapphire laser system JETI, delivering pulses with 28 fs pulse duration at a central wavelength λ of 800 nm with a pulse energy E_L of 500 mJ on target. The laser was focussed by an off-axis parabola with an incidence angle α to the surface normal of 13° to a spot of $3.6 \mu\text{m}$ FWHM diameter. Thus, the intensity I in the focal spot was $1.8 \times 10^{20} \text{ W/cm}^2$, corresponding to an amplitude of the normalized vector potential of $a_0 = (eE_L)/(m_e c \omega) = \sqrt{(I\lambda^2)/(1.37 \times 10^{18} \text{ W cm}^2 \mu\text{m}^2)} \approx 9$. The targets were 5 and $25 \mu\text{m}$ thick titanium foils, both coated with a $1 \mu\text{m}$ thick layer of silicon monoxide. They could be moved in two directions via translation stages, allowing for ~ 200 laser pulses on one target. Beside the X-ray spectroscopy, also the ion energy spectra²⁶ were recorded, allowing for an independent determination of the TNSA field. The ion spectrometer comprises

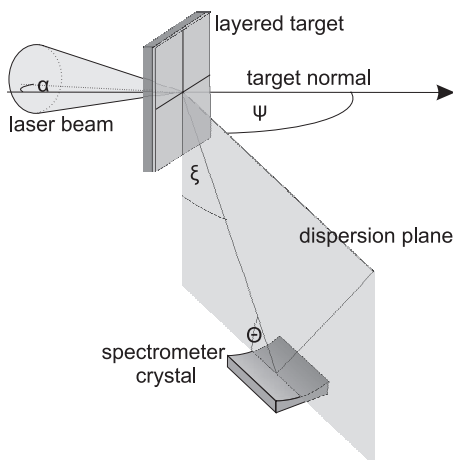


FIG. 4. Target and spectrometer geometry used in the experiment.

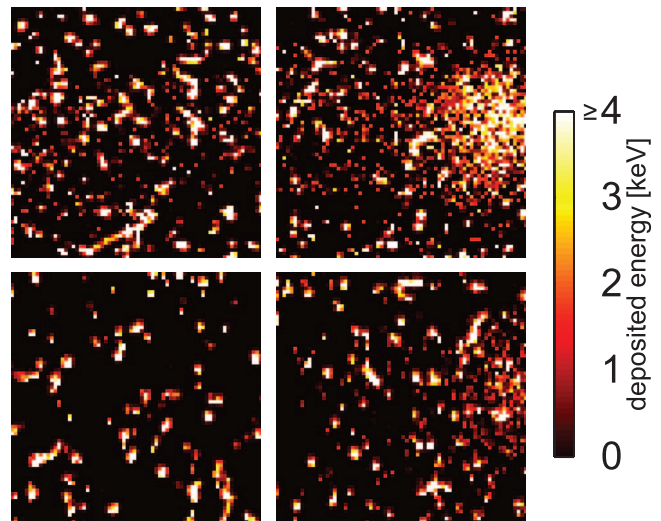


FIG. 5. Parts (100×100 pixel) of single pulse CCD images for $5 \mu\text{m}$ (upper row) and $25 \mu\text{m}$ (lower row) thick targets. Both targets have an $\approx 1 \mu\text{m}$ thick silicon monoxide layer on the rear side. The right column shows the parts of the images recording the $K\alpha$ emission, the left column shows parts recording the emission at lower energies.

a Thomson parabola as dispersive element and a MCP detector for online observation of the spectra. Thus, for every pulse we simultaneously recorded a proton- and an X-ray spectrum. The spectral range of the X-ray spectra is limited by the CCD size and not by the crystal size, and can thus be adjusted by moving the CCD along the cylinder axis of the spectrometer crystal. It was set to cover the emission from 1660 to 1760 eV.

In Figure 5, we show typical X-ray CCD images recorded for single laser pulses from both targets. The count rate in each pixel is proportional to the absorbed photon energy. The scale ranges from a count rate corresponding to 0 eV photon energy (black) to 4000 eV photon energy (white). This is only a small part of the entire dynamic range of the CCD. By analyzing the charge in each pixel, the impinging photon energy could be deduced within the energy resolution of ~ 160 eV. Most of the events in the image arise from the background, produced by hard bremsstrahlung of the highly energetic electrons and secondary effects. Only very few events are diffracted by the crystal and contribute to the spectrum. In the region recording the $K\alpha$ emission, more than one signal photon hit one CCD-pixel. The rest of the spectrum could be recorded in the single photon counting regime only for the $25 \mu\text{m}$ thick target. Thus, the spectra were processed in two different ways: first, only pixels containing a charge corresponding to 1700 ± 220 eV photon energy, were taken into account. This method, referred as single photon counting in the following, reduces the background most efficiently. But it requires a sufficiently small photon flux, which was not the case for the whole spectrum for the thin target, and the $K\alpha$ emission for the thick target. The second treatment was to only remove the events on the image that were produced by photons above a certain threshold, which was chosen with respect to the maximum number of $K\alpha$ photons hitting one pixel, namely, 8 and 3 for the 5 and $25 \mu\text{m}$ thick targets, respectively. The remaining background was determined from a part of the image not containing the spectrum. This treatment

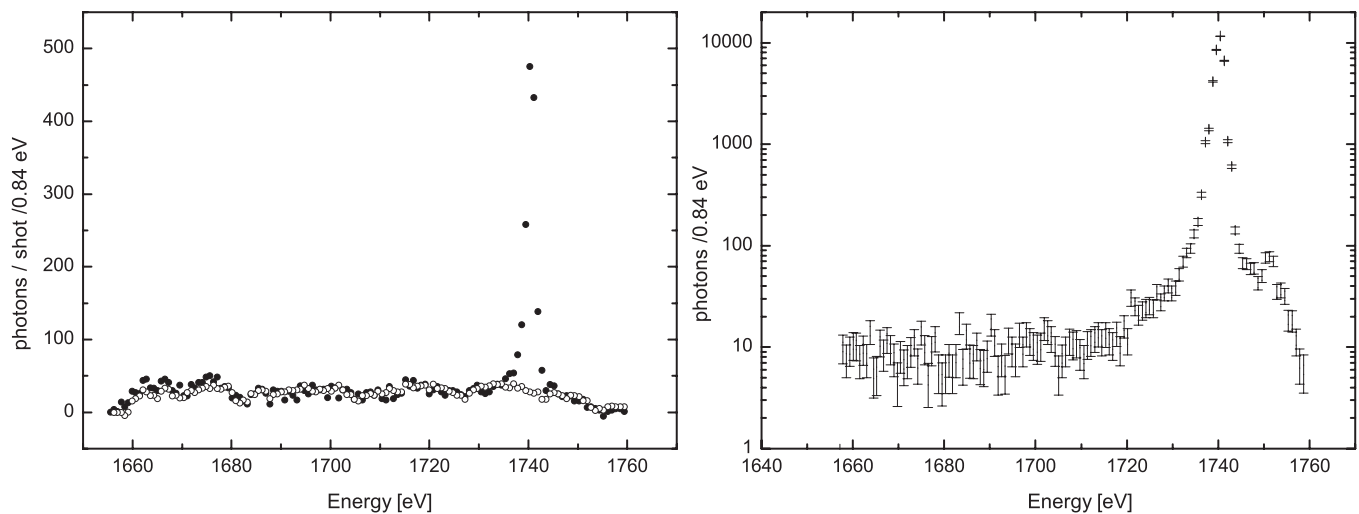


FIG. 6. (a) Spectra from the $5 \mu\text{m}$ targets with (full symbols) and without (open symbols) silicon layer. These spectra were accumulated over 208 and 187 laser pulses, respectively. The errors of the photon counting statistics are smaller than the symbols. (b) Spectrum from a $25 \mu\text{m}$ thick target, accumulated over 135 laser pulses.

produces a significantly higher noise. To obtain the spectra, the images were then summed up in the horizontal direction and slightly binned in the dispersion direction, according to the spectrometer resolution. It should be noted that the spectral resolution of the instrument is not affected by both procedures, since the spectrum is deduced from the position on the CCD.

In Figure 6, we show the spectra from both targets. The thin target exhibits a strong continuous emission in the whole recorded spectral range. This could be attributed to the bremsstrahlung emission from the front side plasma, since it is also present in the spectrum from the uncoated target.

This background amounts for almost 1/10 of the $K\alpha$ emission, making it impossible to detect the forbidden transition. It is more efficiently reabsorbed in the $25 \mu\text{m}$ thick target (more than 5 orders of magnitude), making it possible to record the spectrum beside the $K\alpha$ line in the single photon counting regime and thus with a very high dynamic range. The spectrum for the thick target is composed of the spectra from the different evaluation schemes. The $K\alpha$ emission is evaluated with the method of hard events deleting the rest of the spectrum with the single photon counting method. The shoulder on the high energy side of the $K\alpha$ emission is the spectrally shifted $K\alpha$ line from Si(VII) ions, which is actually cut a bit by the entrance aperture of the spectrometer. The enhancement of the $K\alpha$ blue wing could be explained by a different ionization state of the Si ions for laser pulses where protons were detected compared to pulses with no accelerated protons. The dynamic range of the spectrum clearly exceeds the requirements deduced from the simulations. Nevertheless, we were not able to detect the L_1 -K satellite for several reasons. The major one was a prepulse problem of the laser, leading to an electric field strength behind the target much weaker than expected. The proton energies did not exceed 0.3 MeV, in contrast to the expected values of 3–4 MeV, and proton spectra could not be detected except for a few laser pulses. Thus, also the electric fields were much smaller than expected. This prepulse also explains the unexpected large amount of contin-

uous emission from the front side plasma. In an experiment with a steeper initial density gradient, one could expect a reduced electron temperature, less coupling of laser energy into accelerated electrons as well as less free-free continuum emission. Thus, also the bremsstrahlung emission in the relevant 1.7 keV range, to be reduced greatly.²⁷

But, since we recorded proton- and X-ray spectra for every single shot, the X-ray spectra could be discriminated against the proton spectra. In Figure 7, two spectra are shown for laser pulses where protons were both detected and not detected. For each of them, 15 laser pulses were accumulated. There are significant differences in the wings of the $K\alpha$ emission of the spectra where we could simultaneously detect protons and where we could not. To be specific, there are more

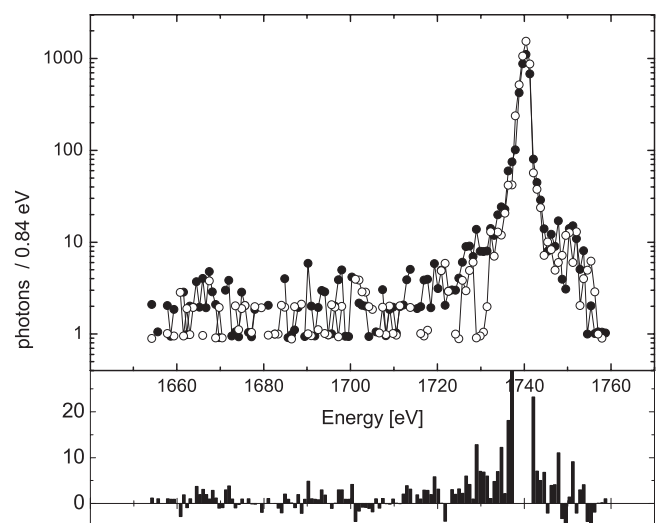


FIG. 7. Si $K\alpha$ emission from $1 \mu\text{m}$ SiO at the rear side of $25 \mu\text{m}$ Ti. Spectra from laser pulses where protons were detected (full symbols) are compared with spectra from laser pulses, where no protons were detected (open symbols), for both spectra 15 laser pulses were accumulated. The lower panel shows the difference of the two (protons detected—no protons detected), indicating a line broadening.

photons in these wings in the spectra from the pulses, where also a proton signal was detected. These differences amount to 87 ± 20 photons in the part of the spectrum between 1730 and 1737 eV, and 73 ± 19 photons in the range between 1742 and 1749 eV. Since these errors give the variance of the photon statistic, these differences amount to more than 3σ .

To exclude that these additional photons in the laser pulses where protons were detected originate in an altered background, it was checked that these differences do not depend on the selection of the pulses for the reference spectrum (without proton detection). Therefore, the hard X-ray (> 100 keV) dose was used that was also recorded for every shot. The spectrum shown is from randomly picked pulses, for another one 15 pulses were used, that produced a hard X-ray dose similar to the 15 pulses with proton detection and for a third one the 15 pulses were selected that produced the highest hard X-ray dose. For all three samples, the results, i.e., the difference photon number in the $K\alpha$ wings, are consistently similar.

It was also checked that these additional photons in the $K\alpha$ wings from the 15 pulses with proton detection do not only originate from one or a few “cautious” pulses. It was found that they are indeed uniformly distributed over the 15 pulses.

Thus, there is a correlation between the detection of accelerated protons, which indicates the presence of the TNSA field, and modifications in the silicon emission spectra. But as pointed out above it is hardly possible to infer the field strengths from the modifications of the $K\alpha$ line profiles. This spectral region is also affected by other effects, like satellites from different ionization states²⁸ or magnetic fields, that are expected inside the target²⁹ and at the interface between the two layers.³⁰ The influence of expected line broadening by the Zeeman splitting induced by magnetic fields of several hundreds of Tesla as measured by Gizzi *et al.* is in the order of μ_B 0.16 eV, which is 1/10 of the measured line FWHM.

V. CONCLUSION

We present a method to measure the TNSA fields, based on modifications of inner shell emission spectra of atoms exposed to these fields. We developed a spectrometer capable of recording the emission of a silicon tracer layer at the rear side of a high intensity laser irradiated foil. In this setup, a cylindrically bent PET crystal is coupled to a CCD camera, allowing for single photon counting. This allows for recording spectra with a high dynamic range by accumulation of a moderate number of laser pulses. By simultaneously measuring the proton and the X-ray spectra for every single pulse, it is possible to correlate these two signals.

ACKNOWLEDGMENTS

We would like to acknowledge the laser support by the JETI laser crew and the Deutsche Forschungsgemeinschaft

(Contract No. TR18), the BMBF (Contract No. 03ZIK445, onCOOPtics), LASERLAB Europe, and COST (MP 0601).

- ¹S. C. Wilks, A. B. Langdon, T. E. Cowan, M. Roth, M. Singh, S. Hatchett, M. H. Key, D. Pennington, A. MacKinnon, and R. A. Snavely, *Phys. Plasmas* **8**, 542 (2001).
- ²M. Tatarakis, I. Watts, F. Beg, E. Clark, A. Dangor, A. Gopal, M. Haines, P. Norreys, U. Wagner, M. Wei, M. Zepf, and K. Krushelnick, *Nature (London)* **415**, 280 (2002).
- ³B. Remington, R. Drake, H. Takabe, and D. Arnett, *Phys. Plasmas* **7**, 1641 (2000).
- ⁴J. Lindl, *Phys. Plasmas* **11**, 3933 (1995).
- ⁵O. Jäckel, J. Polz, S. M. Pfotenhauer, H.-P. Schlenvoigt, H. Schwoerer, and M. C. Kaluza, *New J. Phys.* **12**, 103027 (2010).
- ⁶P. Antici, J. Fuchs, M. Borghesi, L. Gremillet, T. Grismayer, Y. Sentoku, C. d’Humières, E. Cecchetti, A. Mančić, A. C. Pipahl, T. Toncian, O. Willi, P. Mora, and P. Audebert, *Phys. Rev. Lett.* **101**, 105004 (2008).
- ⁷M. Borghesi, *Phys. Plasmas* **9**, 2214 (2002).
- ⁸T. Sokollik, M. Schnürer, S. Ter-Avetisyan, P. Nickles, E. Risse, M. Kalashnikov, W. Sandner, G. Priebe, M. Amin, T. Toncian, O. Willi, and A. Andreev, *Appl. Phys. Lett.* **92**, 091503 (2008).
- ⁹A. Mackinnon, P. Patel, R. Town, M. Edwards, T. Phillips, S. Lerner, D. Price, D. Hicks, M. Key, S. Hatchett *et al.*, *Rev. Sci. Instrum.* **75**, 3531 (2004).
- ¹⁰K. Quinn, P. Wilson, B. Ramakrishna, L. Romagnani, G. Sarri, C. Cecchetti, L. Lancia, J. Fuchs, A. Pipahl, T. Toncian *et al.*, *Rev. Sci. Instrum.* **80**, 113506 (2009).
- ¹¹P. Mora, *Phys. Rev. Lett.* **90**, 185002 (2003).
- ¹²U. Rebhan, N. Wiegart, and H. Kunze, *Phys. Lett. A* **85**, 228 (1981).
- ¹³K. Tsigutkin, R. Doron, E. Stambulchik, V. Bernshtam, Y. Maron, A. Fruchtman, and R. Comisso, *Phys. Rev. E* **76**, 046401 (2007).
- ¹⁴E. Stambulchik and Y. Maron, *J. Instrum.* **6**, P10009 (2011).
- ¹⁵M. Gu, *Astrophys. J.* **582**, 1241 (2003).
- ¹⁶E. Stambulchik and Y. Maron, *Phys. Rev. A* **56**, 2713 (1997).
- ¹⁷M. Lontano and M. Passoni, *Phys. Plasmas* **13**, 042102 (2006).
- ¹⁸E. Stambulchik, V. Bernshtam, L. Weingarten, E. Kroupp, D. Fisher, Y. Maron, U. Zastra, I. Uschmann, F. Zamponi, E. Förster *et al.*, *J. Phys. A: Math. Theor.* **42**, 214056 (2009).
- ¹⁹J. Hoszowska, J. Dousse, D. Castella, J. Corminboeff, Y. Kern, and P. Raboud, *J. Phys. B* **33**, 3165 (2000).
- ²⁰F. Livet, F. Bley, J. Mainville, R. Caudron, S. G. J. Mochrie, E. Geissler, G. Dolino, D. Abernathy, G. Grübel, and M. Sutton, *Nucl. Instrum. Methods Phys. Res. A* **451**, 596 (2000).
- ²¹F. Zamponi, T. Kämpfer, A. Morak, I. Uschmann, and E. Förster, *Rev. Sci. Instrum.* **76**, 116101 (2005).
- ²²C. Fourment, N. Arazam, C. Bonte, T. Caillaud, D. Descamps, F. Dorchie, M. Harmand, S. Hulin, S. Petit, and J. J. Santos, *Rev. Sci. Instrum.* **80**, 083505 (2009).
- ²³R. Hall, M. Lewis, B. Leigh, and K. Evans, *X-Ray Spectrom.* **8**, 19 (1979).
- ²⁴H. Chen, B. Soom, B. Yaakobi, S. Uchida, and D. D. Meyerhofer, *Phys. Rev. Lett.* **70**, 3431 (1993).
- ²⁵M. Dirksmüller, O. Rancu, I. Uschmann, P. Renaudin, C. Chenais-Popovics, J. Gauthier, and E. Förster, *Opt. Commun.* **118**, 379 (1995).
- ²⁶S. Pfotenhauer, O. Jäckel, J. Polz, S. Steinke, H. Schlenvoigt, J. Heymann, A. Robinson, and M. Kaluza, *New J. Phys.* **12**, 103009 (2010).
- ²⁷S. Bastiani, A. Rousse, J. Geindre, P. Audebert, C. Quiox, G. Hamoniaux, A. Antonetti, and J. Gauthier, *Phys. Rev. E* **56**, 7179 (1997).
- ²⁸U. Zastra, P. Audebert, V. Bernshtam, E. Brambrink, T. Kaempfer, E. Kroupp, R. Loetzsch, Y. Maron, Y. Ralchenko, H. Reinholz, G. Roepke, A. Sengebusch, E. Stambulchik, I. Uschmann, L. Weingarten, and E. Foerster, *Phys. Rev. E* **81**, 026406 (2010).
- ²⁹F. Zamponi, “Electron propagation in solid matter as a result of relativistic laser plasma interactions,” Ph.D. thesis (Friedrich-Schiller-University, Jena, 2007).
- ³⁰L. A. Gizzi, S. Betti, E. Förster, D. Giulietti, S. Höfer, P. Köster, L. Labate, R. Löttsch, A. P. L. Robinson, and I. Uschmann, *Phys. Rev. ST Accel. Beams* **14**, 011301 (2011).